

Blind deconvolution with principal components analysis for wide-field and small-aperture telescopes

Peng Jia,^{1,2★} Rongyu Sun,^{3★} Weinan Wang,¹ Dongmei Cai¹ and Huigen Liu⁴

¹College of Physics and Optoelectronics, Taiyuan University of Technology, Taiyuan 030024, China

²Department of Physics, Durham University, South Road, Durham DH1 3LE, UK

³Purple Mountain Observatory, Chinese Academy of Sciences, Nanjing 210008, China

⁴School of Astronomy and Space Science, Nanjing University, Nanjing 210023, China

Accepted 2017 May 26. Received 2017 May 19; in original form 2016 November 24

ABSTRACT

Telescopes with a wide field of view (greater than 1°) and small apertures (less than 2 m) are workhorses for observations such as sky surveys and fast-moving object detection, and play an important role in time-domain astronomy. However, images captured by these telescopes are contaminated by optical system aberrations, atmospheric turbulence, tracking errors and wind shear. To increase the quality of images and maximize their scientific output, we propose a new blind deconvolution algorithm based on statistical properties of the point spread functions (PSFs) of these telescopes. In this new algorithm, we first construct the PSF feature space through principal component analysis, and then classify PSFs from a different position and time using a self-organizing map. According to the classification results, we divide images of the same PSF types and select these PSFs to construct a prior PSF. The prior PSF is then used to restore these images. To investigate the improvement that this algorithm provides for data reduction, we process images of space debris captured by our small-aperture wide-field telescopes. Comparing the reduced results of the original images and the images processed with the standard Richardson–Lucy method, our method shows a promising improvement in astrometry accuracy.

Key words: methods: data analysis – techniques: image processing – astrometry.

1 INTRODUCTION

In the era of time-domain astronomy, a large amount of data from celestial objects are obtained at multiple wavebands every day. These data are used to study temporally changing astronomical objects (Wang et al. 2009). Due to different temporal scales, continuous observations are required (Grindlay et al. 2012; Kelly et al. 2014). In the optical band, telescopes with wide fields of view and small apertures are an appropriate choice (Burd et al. 2005), because the wide field of view provides wide sky coverage, and because using small apertures reduces the manufacturing cost of multiple telescopes located at different sites (increasing temporal and sky coverage) (Kaiser et al. 2002). However, increasing the field of view of these telescopes will increase optical design complexity, and introduce additional refractive components (Ackermann, McGraw & Zimmer 2010).

For wide-field small-aperture telescopes, different factors, such as the dispersion of refractive material, misalignment of components during observation and imperfect optical surfaces, will

introduce significantly more complex and serious aberrations than those of ordinary reflector telescopes, such as the classical Cassegrain telescope with a small field of view (Wilson 1996). Moreover, as these telescopes are generally working as robotic telescopes with no active or adaptive optics systems (Babcock 1953; Mast & Nelson 1982), atmospheric turbulence and thermal and gravity deformation of the telescope mirror or lens will further result in dynamical aberrations (Smith 2000; Lemaitre 2009). These aberrations will lead to spatial and temporal variations in telescope optical quality, and introduce highly variable point spread functions (PSFs) in different parts of different images (Jee & Tyson 2011; Chang et al. 2012). These PSF variations will result in a distorted final image, reducing the effective resolution and signal-to-noise ratio (SNR) of faint objects, which can become undetectable. Astrometric and photometric precision is also reduced.

To increase image quality, we need to reduce the side effects due to the variable PSFs. Image deconvolution is a well-established post-processing method that does not require any instrumental modification or change to observing strategy, and it can be used with historical data (Starck, Pantin & Murtagh 2002). When the PSF of the whole optical system is known, deconvolution recovers the original image with some regularized conditions and for example,

* E-mail: robinmartin20@gmail.com (PJ); rysun@pmo.ac.cn (RS)

has shown impressive results in processing images captured by the *Hubble Space Telescope* (Adorf, Hook & Lucy 1993). For optical ground-based telescopes, due to the atmospheric turbulence, PSFs of different images are highly variable and it is hard to get an effective PSF for deconvolution. For these images, blind deconvolution was proposed to simultaneously recover the original image as well as the PSF (Ayers & Dainty 1988; Bertero & Boccacci 2000; Desiderà & Carbillat 2009; Prato et al. 2013). However, to reduce computational complexity, the PSF is assumed to be spatial-invariant in these methods. This assumption does not match the reality for most ground-based observations, because aberrations due to atmospheric turbulence and those from the optical system are different for different field directions (Lukin 1995). Under these circumstances, dividing the image into small regions, where the PSFs are assumed to be invariant, and applying blind deconvolution in these small regions is a direct solution. Based on this method, an algorithm called PATCH is proposed (Ciliegi et al. 2014), which shows promising results for processing images captured by telescopes equipped with adaptive optics systems. Astrometry and photometry results are improved after blind deconvolution (La Camera et al. 2015).

However, for images captured by wide-field small-aperture telescopes, it is hard to apply the PATCH method for two reasons: first, the small area inside which the PSF is assumed to be invariant is several arcsecs (Britton 2006) but it is equivalent to only several pixels in the wide-field images, which is too small for restoration. Secondly, the low CCD sampling rate smooths the differences between PSFs and expands the size of the PSF-uniform area but it is not clear how much the size increases. These facts make it hard to set a suitable size for PATCH. A convenient way is to assume that the PSFs are spatial-invariant and to deconvolve the images with a spatial-invariant artificial PSF and conventional algorithm (Fors et al. 2010; Sun & Zhao 2014; Núñez et al. 2015). However, the restoration results are unstable in these algorithms, because the initial PSF is chosen according to experience. If the differences between PSFs in the whole image and the artificial PSF are small, it is possible for conventional deconvolution to find a PSF that will increase image quality. However, as the PSF has many pixels, there are complex non-linear relations between the quality evaluation of the image and PSF. The optimization algorithms in conventional deconvolution algorithms mainly use linear space (Sun & Yuan 1997), hence the quality of the restored images varies dramatically. To improve blind deconvolution results, we should use an initial guess for a PSF that is close to the PSFs in the whole image and use an appropriate PSF search method for blind deconvolution.

The aforementioned PSF projection technique can also be seen as PSF regularization. There are two such methods. The first method is modelling the PSF with parameters according to the physical process of the imaging system (Jia, Cai & Wang 2014). However, due to complicated aberrations in wide-field telescopes and the complexity of initial PSF parameter tuning, this method is not practical for image restoration. The second method is modelling the PSF according to its statistical properties. To ensure that this model is numerically stable and can properly represent different PSF patterns, a large number of diversely distributed PSFs are required (Theodoridis & Koutroumbas 2008). For wide-field small-aperture telescopes, because there are a large number of stars distributed diversely in each frame of an image and there are a large number of images captured continuously with almost the same exposure time, it is possible to generate the PSF manifold space from these data through a statistical method for PSF projection.

In this paper, principal component analysis (PCA) will be used for PSF projection. PCA is a generalized multivariate data analysis method that minimizes the mean square error of the whole data set, showing promising properties for data packaging and dimension reduction (Vidal, Ma & Sastry 2016). It is applied to decomposed and reconstructed PSFs in different fields of view for both space and ground-based telescopes (Lupton et al. 2001; Jee et al. 2007; Jee & Tyson 2011). We classify all the PSFs represented by the PCA components with unsupervised learning (Haykin 2010). According to the classification results, images will be divided into different cubes and one frame of the images in each cube will be used to compute a mean PSF, which will be used as a prior PSF. A modified version of scaled gradient projection (SGP) based blind deconvolution (Prato et al. 2013) with the prior PSF will then be used to restore the image.

In Section 2, we will discuss the concept and method of our techniques. In Section 3, we will process a series of images from three of our telescopes and show the improvement in astrometry accuracy. In Section 4, we will discuss the shortcomings of our method and anticipated future work.

2 BASIC PRINCIPLE AND METHOD

The physical process of imaging in wide-field small-aperture telescopes can be expressed by

$$I(x, y) = [O * \text{PSF}(x, y)]_{\text{Pixel}(x, y)} + N(x, y). \quad (1)$$

O is the original image, I is the observational image and $*$ stands for convolution. $\text{PSF}(x, y)$ is the PSF of the whole optical system and since the PSF is spatially variable, it is different for different (x, y) . $[\]_{\text{Pixel}(x, y)}$ is the discretization process and it also includes the pixel response function of pixel (x, y) . $N(x, y)$ is noise from the CCD, shot noise and sky background. When only $I(x, y)$ is known and $N(x, y)$ and O are partly known, blind deconvolution can restore $O(x, y)$ through optimization under some regularization conditions.

Optimization is also a search process, and blind deconvolution can be viewed as a problem of finding an optimal point in the manifold space spanned by all the possible vectors of the PSF and the image. The regularization conditions restrict the dimension and the geometric property of the manifold space. The dimension and geometric properties of the manifold space will lead to different levels of problem complexity.

Since the PSF is directly related to the physical process of imaging and because the physical and geometrical optics of imaging have already been previously studied (Fischer et al. 2000; Gonzalez & Woods 2002), regularization of a PSF with imaging theory is a commonly used technique (Campisi & Egiazarian 2016). However, unlike diffraction-limited images, PSFs obtained by wide-field small-aperture telescopes are highly variable, under-sampled and strongly affected by the sky background (Popowicz & Smolka 2015) and CCD noise (Popowicz et al. 2016). Under these circumstances, the size of the PSF is discretized to just a few pixels, which makes the pixel response function much more important than for diffraction-limited images. The low spatial sampling, as well as the high sky background noise, make the wings of the PSF unrecognizable. To generate a PSF model for PSF regularization with blind deconvolution, we need to take these effects into consideration and furthermore we also need to calibrate every detector pixel to provide an accurate PSF model (Piotrowski et al. 2013). Such a calibration is impractical for our telescopes, because the instruments have already been commissioned and the data collected.

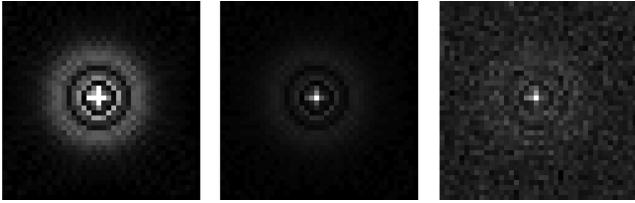


Figure 1. Monte Carlo simulation of the PSF of stars with different magnitudes. The left-hand panel shows a star with a magnitude of 8, the middle panel shows a star with a magnitude of 10 and the right-hand panel shows a star with a magnitude of 13. The sky background has a magnitude of 15. The x - and y -axes in these figures are in pixels and the total number of pixels in each of these directions is 40.

Another method for PSF regularization considers PSFs to be images with specific structure, and models the PSFs according to their statistical properties. In this method, to keep the model statistically effective, a large number of diversely distributed PSFs are required to include all possible modes. For the telescopes we used to collect our data, a large field of view and large number of images will provide a large number of diversely distributed PSFs in the final images. The low CCD sampling rate will smooth the high-order spatial variation in PSFs, which will increase statistical effectiveness and reduce the number of required modes for PSF representation as well. In this paper, out of all the statistical description methods, we select PCA for its computational simplicity. For real applications, large numbers of PSFs that satisfy certain conditions will be subtracted from all the observational data or telescope calibration data, depending on the observation mode, and PCA will be used to construct a manifold space with these PSFs. In the manifold space, PSFs presented by the PCA basis in different images will be clustered with a self-organizing map (SOM) (Kohonen 1982). According to the cluster results, images with the same type of PSFs will be divided into small regions. The mean PSF of the same type of PSFs (i.e. of each small clustered region) will be used as the prior PSF for this region and we will use a modified SGP method to restore images.

We will discuss the PSF selection in Section 2.1, the generation of the PSF feature space in Section 2.2, PSF classification in Section 2.3, and PSF regularization and blind deconvolution in Section 2.4.

2.1 PSF selection for feature generation

Because there is a large number of stars in the final images from wide-field telescopes and the images of these stars are just point sources before they are modulated by the atmosphere, telescope and camera, it is possible to use them to extract information about the PSFs of the whole image system. In most optical observations, besides the aberrations induced by atmospheric turbulence and the optical system, the main factors that affect the PSF shape are the sky background noise, CCD pixel scale and the depth of the CCD full well limitation. The shapes of PSFs should be the same if there are enough pixels in images of stars that are not saturated and the SNR is high enough, and they can be used as a reference PSF like the ordinary PSF shown in Figs 1 and 2.

However, for our applications, due to the low CCD sampling rate (several arcsecs per pixel), high background noise and complicated aberrations in the telescopes, there are very few bright stars that can be used as reference PSFs, as shown in Fig. 3. When there are not enough stars with a high SNR, we will select stars with a relatively low SNR as references. In this circumstance, it is important to notice

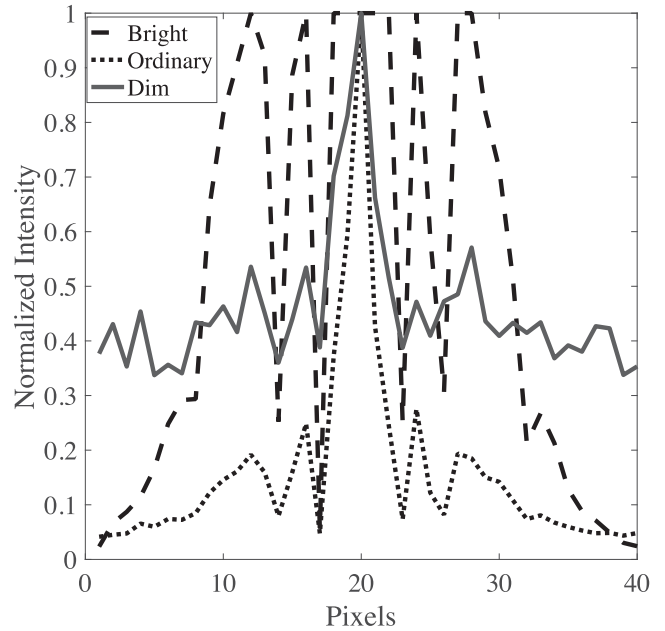


Figure 2. The 1D curve of the PSFs in Fig. 1. The peak values of the PSFs are normalized for demonstration. As can be seen, when a star is too bright, the peak of the PSF will be flattened due to saturated pixels and when the star is too dim, the wing of the PSF will not be observable due to the high background.

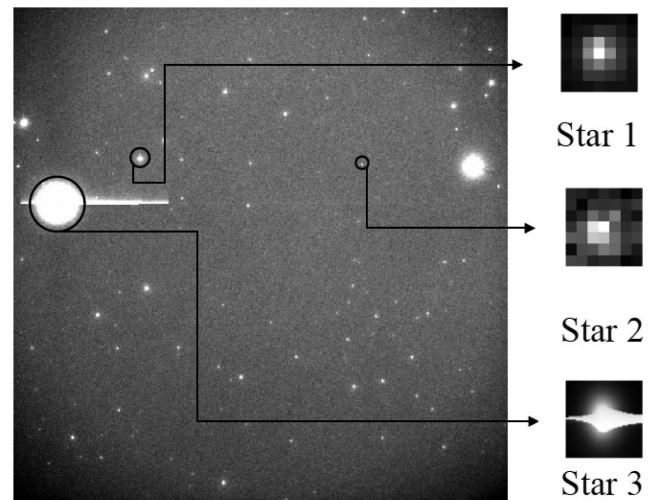


Figure 3. One frame of images from our telescopes. For better display, the grey-scale in this figure is adjusted with the IRAF zscale algorithm in DS9 (Smithsonian Astrophysical Observatory 2000). Star 1 has a SNR of 22.31, star 2 has a SNR of 5.23 and star 3 has a SNR of 72.83. We set the SNR as $(S - B)/\sigma$, where S is the mean pixel value of the investigated star image, B is the mean grey-scale value of the background image and σ is the noise level. The full well depth for our CCD is 16 383 and the maximal value in the image is around 11 000 (the bright stripe is a defect caused by the high frame rate of the CCD during observation). To get better blind deconvolution results, we should select PSFs by considering the SNR of stars as well as the number of stars with these PSFs. Generally, star 1 will be selected as the PSF reference, because it has a relatively high SNR and there are lots of stars with SNR close to that of star 1.

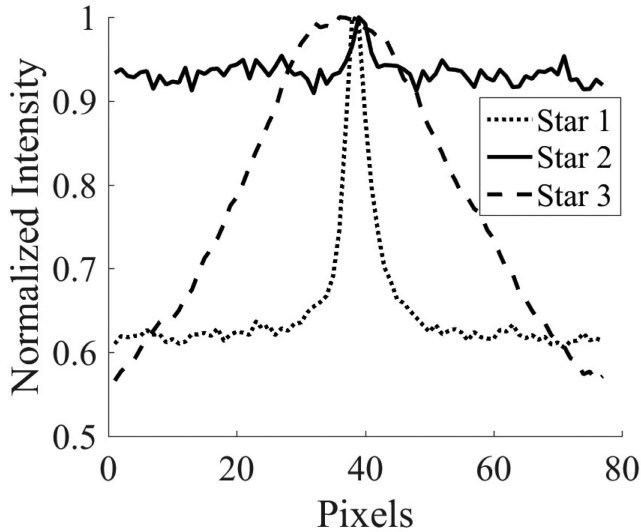


Figure 4. The 1D curve of the PSFs in Fig. 3. The peak values of the PSFs are normalized for demonstration. Most reference stars in our observational data have a 1D curve like star 1. When comparing the PSFs of different stars, we find that their shapes are approximately modified by the background noise.

that stars with a different magnitude will show different shapes even though their optical PSFs are the same, mainly due to the high background noise as shown in Fig. 4. Based on our experience, we will select stars with a relatively high SNR, moderate magnitude (the differences in the magnitudes of these stars are limited to 3 mag and the number of stars in this scale is the most) and regular shape (we remove stars with extraordinary ellipticity).

Note that the PSFs can be obtained by two methods according to different observation modes. For sidereal-tracking observations, the PSFs can be obtained directly from the observation data while for other object-tracking observations (such as space debris observations), the PSFs can be obtained by telescope calibration observations (through an observation towards the North Pole with the same exposure time used for the wide-field observations).

2.2 PSF feature generation with PCA

When a large number of PSFs are obtained with the method mentioned in Section 2.1, a classical PCA method can be used for feature generation. Assuming we get N PSFs with $M \times M$ pixels, we will stretch these PSFs into a vector and generate a PSF data matrix \mathbf{S} with $M \times M$ columns and N rows. N should be much larger than $M \times M$ to maintain numerical stability and statistical effectiveness. The PSF data matrix is decomposed by singular value decomposition and then we obtain:

$$\mathbf{S} = \mathbf{U}\mathbf{W}\mathbf{V}^T, \quad (2)$$

where \mathbf{W} is the singular value matrix and \mathbf{U} is the PCA basis matrix (each row of \mathbf{U} is an orthogonal PCA basis). We order the diagonal elements in \mathbf{W} in descending order and calculate the Laplacian of these elements. According to the Laplacian, the components with values greater than a predefined factor (0.001 for this paper) will be selected for PSF presentation, because the relative weight of the effective patterns will decay quickly while the noise pattern will vary slowly. When the noise patterns dominate, the differences in the weight of these patterns will be small and the Laplacian will be close to zero. For wide-field small-aperture telescopes, because of

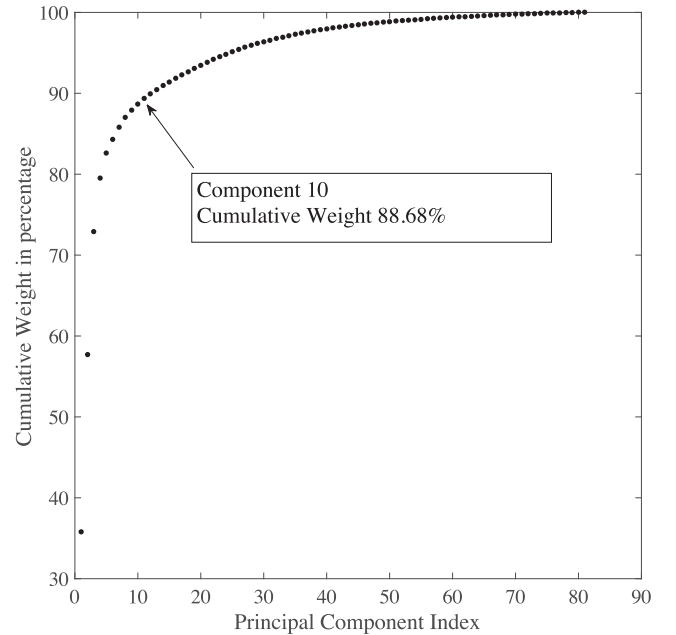


Figure 5. The first 30 PCA components for the PSF basis with a size of 11×11 pixels. This figure shows the contributions of the first 10 components. The cumulative weight of the first 10 components is 88.68 per cent which shows that with only 10 components we can present most of the PSFs with small error.

the low CCD sampling rate and high noise level, the effective PSF pattern will be much smaller than for larger telescopes. As shown in Fig. 5, for ordinary observation data the number of principal effective components is around or less than 10. When the number of reference PSFs is not enough, we can relax the constraint on the star magnitude and use EMPCA for feature generation (Bailey 2012).

2.3 PSF classification with SOM

With the PCA basis generated by the method discussed in Section 2.2, all the PSFs we subtracted from images can be presented with greatly reduced dimensions. For blind deconvolution, these PSFs represented by the PCA components are good starting points to use for PSF difference detection and we can divide images according to the PSF classification results. However, as the number of PSFs is large and classification of these PSFs is a NP-hard problem, it is difficult to classify these PSFs through direct methods.

Classification with large data sets is a common problem in unsupervised machine learning and there are a large number of methods and techniques. In this paper, we choose SOM as the classification method for PSFs because it generates a topographic map of the high-dimensional data, making it easier to interpret in lower dimensions. As we change the dimension of the low-dimension space, it will be easier to discover the continuity of PSFs in the spatial and temporal domain. SOM is widely applied in data classification with high dimensions, such as star and galaxy classification (Maehoenen & Hakala 1995; Miller & Coe 1996), light curve classification (Brett, West & Wheatley 2004; Carrasco Kind & Brunner 2014; Armstrong et al. 2016) and object selection (Geach 2012).

For PSF classification, SOM will map the PSFs using many parameters in the data cube (a cube that includes all the extracted PSFs distributed in the space and time coordinates) to a predefined number of types. In our algorithm, we will classify PSFs with SOM

into a number of different types and calculate the Davies–Bouldin (DB) index for each classification, as defined by:

$$DB = \frac{1}{n} \sum_{i=1}^n \max_{j \neq i} \left(\frac{\sigma_i + \sigma_j}{d(c_i, c_j)} \right), \quad (3)$$

where n is the number of clusters, c_i and c_j are the centres of two clusters, σ is the average distance of all the elements in a cluster to its centre and $d(c_i, c_j)$ is the distance between the centres of two clusters. We will select a PSF with a small DB index and an appropriate number of clusters (generally less than 10) as the PSF cluster with the best results.

With the PSF cluster results, we will be able to give the positions (spatial coordinates for images and temporal coordinate for different frames) of different PSFs with different labels. With these labels, we can calculate the fraction of different PSFs in each image. If most of the PSFs (more than 80 per cent) in one frame or in continuous frames of images have the same label, these images will be grouped as one class of images and the mean PSF will be used as the prior PSF. If there are clusters with PSFs with different labels, these stars will be used as a seed and we will grow the seeded region to generate index images (Adams & Bischof 1994). The index images have the same size as the original images and the values of the pixels in the images are the index number grown from the seeds. Then images or a part of images with the same index will be cut and the mean PSF of the same class will be used as the prior PSF. If the PSFs are highly mixed and no cluster exists, the mean PSF of all the PSFs will be used as the prior for blind deconvolution of all the images.

Different situations for the classification results are shown in Figs 6, 7 and 8. In Fig. 6, the PSFs change continuously in the spatial/temporal domain. The upper right part of different images will be cut into a group and the rest will be cut into another group. In Fig. 7, different types of PSFs are highly mixed together and the mean PSF of all the PSFs will be used for blind deconvolution of all the images. In Fig. 8, a slice of images (from the 9th to the 14th) will be divided from the whole data cube and we will use the mean PSF of these images for blind deconvolution and the mean PSF for the rest of the data cube for deconvolution of the remaining images.

2.4 SGP-based blind deconvolution algorithm for images with a low spatial sampling rate

SGP-based blind deconvolution was proposed for processing images obtained by telescopes with an adaptive optics system. This method uses three constraints for the PSF: the non-negativity, normalization and Strehl ratio. The non-negativity and normalization constraints are used in our algorithm. However, the Strehl ratio constraint is not practical for wide-field telescopes if their apertures are too big, because one pixel in the final image is more than several arcsecs, which is much larger than the Airy disc of the telescope and the seeing disc. So, we modify the original SGP algorithm and set the Strehl ratio limit to 1. Besides, during real applications, we find that there are overfittings of the PSFs after many iterations and early stopping of the iteration is recommended. The best number of iterations is of an order of magnitude around 10 depending on the data quality. When the data quality is good, the image quality will increase when the number of iterations is less than 1000 (1000 is the maximal number of iterations we defined in the function though the image quality may increase if the number of iterations is more than 1000). When the noise level is high, the image quality will stop increasing when the number of iterations is more than 10. For the

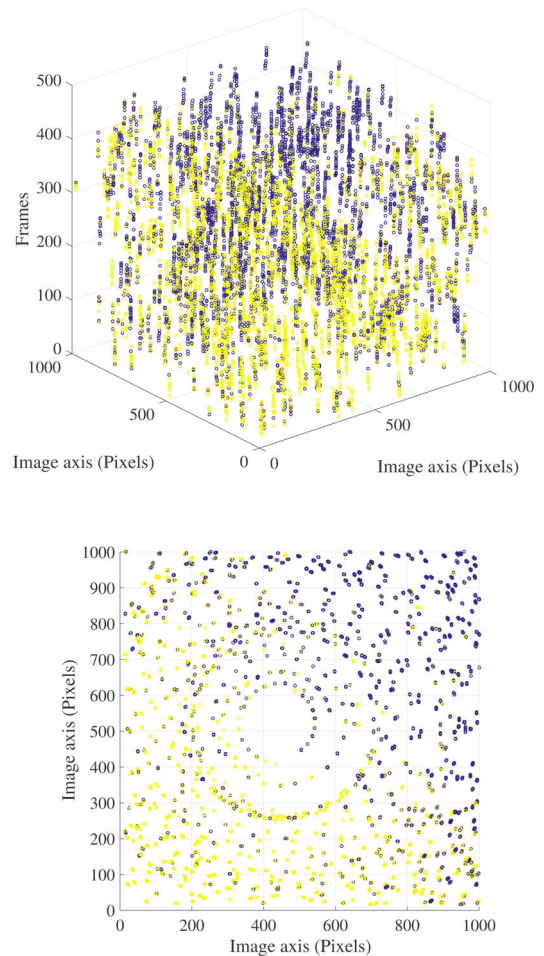


Figure 6. PSF classification results for spatially and temporally continuously variable PSFs. There are 40 000 PSFs in 500 frames of images. For clarity, classification with two kinds is shown. The upper panel is a 3D data cube and the bottom panel is the 3D data cube projected to spatial coordinates. Each frame of these images can be cut into two small images and the mean PSF of these two parts will be used as the prior PSF for blind deconvolution.

robustness of our deconvolution results, we set 10 as the maximal number of iterations.

3 APPLICATION AND RESULTS

3.1 Observation instruments and data

To test the performance of our algorithm, we obtained a series of images utilizing three of our small-aperture telescopes. These telescopes are dedicated to surveying space debris and measuring the corresponding positions. Since space debris comprises fast-moving near-Earth objects, the observing strategy and reduction algorithms are like those adopted for asteroids and comets. However, the relative angular velocity of space debris is generally high (maximum around several arcmins per second) and image degradation is critical, due e.g. to the low SNR caused by limited exposure time, under-sampling and the influence of tracking errors. Hence, space debris is suitable for testing our technique and investigating the improvement of image restoration. Additionally, some objects (e.g. those for laser ranging and navigation) have an ephemeris with extremely high accuracy (Zhang et al. 2012). They have a position

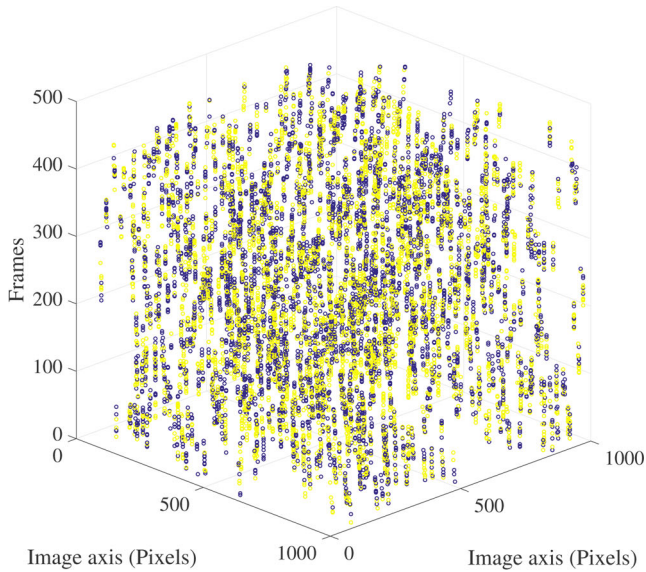


Figure 7. PSF classification results for random variable PSFs. There are 40 000 PSFs in 500 frames of images. For clarity, classification with two kinds is shown. The upper panel is a 3D data cube and the bottom panel is the 3D data cube projected to spatial coordinates. For these images, different kinds of PSFs are mixed together and we will use the average of all the PSFs as the prior PSF for blind deconvolution.

accuracy better than 0.02 arcsec, thus they can be taken as reference positions for astronomical calibrations.

In our application, two GPS satellites with COSPAR (Committee on Space Research) IDs 1996-019A and 2004-009A were observed. During observations, the telescope tracked the object, thus the object appeared at the centre of the whole frame. For one of these observations, continuous images of one object were obtained. A series of these continuous images is called an arc. We obtained 14 arcs including more than 1000 raw CCD images in total. While acquiring the calibration data for blind deconvolution, the observing strategy was alternated. In detail, the calibration data of telescope A were obtained while the telescope was pointing to the North Pole, since it was not able to work robustly under sidereal-tracking mode. The calibration data of telescopes B and C were acquired while the

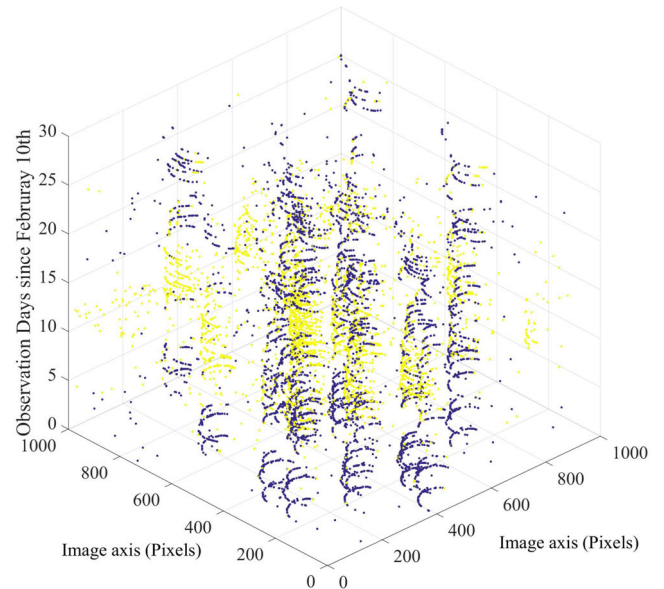


Figure 8. PSF classification results for temporally continuously variable PSFs. There are 10 000 PSFs from observations from February 10 to March 12, 2014. For clarity, classification with two kinds is shown. The upper panel is a 3D data cube and the bottom panel is the 3D data cube projected to temporal-spatial coordinates. In this case, observation data from the 9th day to the 14th day will be cut into a group and the rest of the data will be cut into another group. The mean PSF for these days will be used as the prior PSF for blind deconvolution.

telescopes were sidereal-tracking. The details of these telescopes are listed in Table 1.

3.2 Astrometry results and discussion

3.2.1 Data process and astrometric precision estimation

Once the raw images were obtained, the sources were extracted with the 2D modified moment algorithm (Stone 1989), then these sources were cross-matched with the Tycho2 catalogue (Høg et al. 2000). The equatorial coordinates of the target (one of the two GPS satellites) were derived from the astronomical calibration.

Table 1. Parameters of our telescopes. The exposure time for these telescopes is 2000 ms.

Telescope name	Diameter	Field of view	Frame size	Pixel scale
Telescope A	450 mm	$1.9^\circ \times 1.9^\circ$	1024×1024	6.68 arcsec
Telescope B, C	500 mm	$4.4^\circ \times 4.4^\circ$	2048×2048	7.73 arcsec

Table 2. Comparison of astrometric errors for background stars for different telescopes before and after deconvolution with different methods. Original is the data before deconvolution, Richardson–Lucy is the data after Richardson–Lucy deconvolution with a Gaussian PSF and SGP-PCA is the data after deconvolution with our method. The PSF size used here is 11×11 pixels and the number of iterations in the deconvolution is 10. The number of background stars is the number we obtained for astrometry estimation.

Telescope	Deconvolution algorithm	Number of background stars	Overall rms residual (arcsec)
A	Original	47503	0.4735
	Richardson–Lucy	47458	0.3850
	SGP-PCA	47896	0.3947
B	Original	384619	0.5179
	Richardson–Lucy	393549	0.4779
	SGP-PCA	389885	0.5436

Comparing the measured equatorial coordinates with those derived from the ephemeris, residuals of measurement were obtained. Finally, we took the root mean square (rms) values of all the residuals in one arc as the accuracy of the data reduction.

As discussed in Pascu & Schmidt (1990), the astrometry accuracy of the target depends on the astrometry accuracy of the background stars. In this section, we calculated the astrometry accuracy improvement of the background stars as another test of our method and also as error source analysis for the astrometry results of the target, although there were a large number of reference stars in each frame of our data, which reduced the error caused by the background stars.

We list the astrometry results for two of our telescopes in Table 2. Original is the original astrometry accuracy. Richardson–Lucy is the astrometry accuracy of data processed by Richardson–Lucy deconvolution with a prior Gaussian PSF of 11×11 pixels and 2 pixels full width at half-maximum (FWHM), which was proposed by Núñez et al. (2015). This method improved space debris observation. SGP-PCA is the astrometry accuracy of data processed by our method.

For different telescopes, according to the classification results of the calibration data, different PSF models were used in our method. For telescope A, PSFs of different kinds were randomly distributed (as shown in Fig. 7) and we used the mean PSF as the prior PSF. For telescope B, we found a strong time-dependent variation of PSFs in the whole image as shown in Fig. 12, which indicates that there are some temporal variations of the PSFs in the data from telescope B. However, as the calibration data and observation data were not obtained simultaneously, we could use only the mean PSF from the calibration data as the prior PSF. We processed the data with the methods discussed above and obtained the astrometry results of background stars shown in Table 2.

According to these results, we found:

(1) Both the Richardson–Lucy method and the SGP-PCA method can increase the astrometry accuracy of background stars, when the

Table 3. Original astrometry accuracy for each arc of observation data from telescope A.

Arc ID	rms residual of RA (arcsec)	rms residual of Dec (arcsec)	Overall rms residual (arcsec)
1	1.5715	0.7110	1.7249
2	0.8474	0.4891	0.9784
3	1.5617	0.7737	1.7428
4	1.0673	0.6325	1.2407
5	1.7723	0.6928	1.9029
6	1.0525	0.6512	1.2377
7	1.7924	0.8084	1.9662
8	1.2793	0.5859	1.4071
9	0.9578	0.4507	1.0585
10	2.4581	1.1745	2.7243
11	1.2513	0.7591	1.4635
12	2.1774	1.0684	2.4254
13	1.5027	1.2844	1.9768
14	1.6743	1.1869	2.0523

prior PSF is correct. The astrometry accuracy difference is only 3 per cent for data from telescope A processed by different methods while these methods increase the astrometry accuracy by about 16 per cent.

(2) When the PSF is highly variable, an incorrect PSF model will lead to worse results than those obtained from a simplified universal PSF model.

(3) The astrometry accuracy of background stars can reach better than 0.55 arcsec, which will provide a reliable reference for the astrometry of targets.

3.2.2 Results and Discussion

Although a source of astrometry errors, in Section 3.2.1, we found that the background stars can provide a reliable astrometry reference for targets. In this section, we will show the astrometry improvement for targets for data processed by different methods.

First, we processed data from telescope A. The original astrometry accuracy of the target is shown in Table 3. The rms values of the right ascension (RA) and declination (Dec) residuals are between 0.8 and 2.5 arcsec and the overall rms residuals range between 0.97 and 2.5 arcsec. We used the Richardson–Lucy method with a Gaussian PSF (different size and FWHM of 2 pixels) to process data from telescope A. As shown in Table 4, with the same number of iterations, the astrometry accuracy increases as the size of the PSF increases. The mean astrometry accuracy increases 10.65 per cent with a PSF of 5×5 pixels and 16.07 per cent with a PSF of 11×11 pixels. According to this result, a PSF with a size of 11×11 pixels should be used for the Richardson–Lucy method and the number of iterations for the Richardson–Lucy method should be 10.

For the SGP-PCA method, as shown in Table 5, with the same number of iterations (10 times), the astrometry accuracy increases as the size of the PSF increases: from about 7.58 per cent with a PSF of 5×5 pixels to 41.32 per cent with a PSF of 11×11 pixels. Because PSFs with different sizes will be expanded to give processed images with the same size in SGP, the time difference between deconvolutions with different PSFs is small. We process images with PSFs of 11×11 pixels.

With a PSF of 11×11 pixels, we tested the astrometry accuracy increment with data processed by SGP-PCA method with different numbers of iterations, as shown in Table 6. In this table, we found that the astrometry accuracy will increase as the number of iterations

Table 4. Overall astrometry accuracy in each arc of observation data from telescope A, before and after Richardson–Lucy deconvolution with a Gaussian PSF (FWHM of 2 pixels).

Arc ID	PSF size				Original
	11 × 11 pixels (arcsec)	9 × 9 pixels (arcsec)	7 × 7 pixels (arcsec)	5 × 5 pixels (arcsec)	
1	1.4611	1.4641	1.4710	1.5319	1.7249
2	0.7494	0.7498	0.7551	0.7605	0.9784
3	1.3752	1.3802	1.4142	1.4423	1.7428
4	0.9868	0.9896	1.0014	0.9942	1.2407
5	1.6534	1.6562	1.6808	1.7166	1.9029
6	0.9793	0.9883	0.9745	0.8965	1.2377
7	1.6248	1.6340	1.6865	1.7301	1.9662
8	1.3435	1.3366	1.3593	1.4383	1.4071
9	1.0219	1.0147	1.0289	1.0031	1.0585
10	2.2278	2.2965	2.4069	3.0291	2.7243
11	1.1914	1.1982	1.2514	1.3440	1.4635
12	1.9851	1.9972	2.1272	2.2968	2.4254
13	1.6687	1.7149	1.6429	1.6470	1.9768
14	1.7459	1.7431	1.7886	1.8970	2.0523

Table 5. Overall astrometry accuracy in each arc of observation data from telescope A, before and after deconvolution with our method (with 10 iterations).

Arc ID	PSF size				Original
	11 × 11 pixels (arcsec)	9 × 9 pixels (arcsec)	7 × 7 pixels (arcsec)	5 × 5 pixels (arcsec)	
1	0.5875	0.6972	1.0784	1.6174	1.7249
2	0.5887	0.6387	0.7704	0.9120	0.9784
3	0.8417	0.7995	0.8999	1.4658	1.7428
4	0.7203	0.8012	0.8712	1.0963	1.2407
5	0.7685	0.8053	1.1836	1.7635	1.9029
6	0.7752	0.7372	0.9516	1.2406	1.2377
7	0.8254	0.8928	1.2379	1.8494	1.9662
8	0.6606	0.9060	1.1677	1.4303	1.4071
9	1.4380	0.7234	0.8860	1.1163	1.0585
10	0.8718	1.4012	1.7931	2.2140	2.7243
11	1.6219	0.9451	1.0687	1.3662	1.4635
12	1.5962	1.5113	1.6443	2.3032	2.4254
13	1.4782	1.4782	1.4883	1.8130	1.9768
14	1.2512	1.2524	1.4741	1.9025	2.0523

Table 6. Overall astrometry accuracy in each arc of observation data from telescope A with our method with a PSF size of 11 × 11 pixels.

Arc ID	Number of iterations				Original
	1000 (arcsec)	300 (arcsec)	100 (arcsec)	10 (arcsec)	
1	1.4053	1.0133	0.7127	0.5875	1.7249
2	0.7271	0.6515	0.5679	0.5887	0.9784
3	1.5310	1.3280	1.1190	0.8417	1.7428
4	0.9837	0.7299	0.6401	0.7203	1.2407
5	1.3322	0.7034	0.5895	0.7685	1.9029
6	1.9272	1.4620	1.1256	0.7752	1.2377
7	1.4067	0.9412	0.7636	0.8254	1.9662
8	0.6976	0.7222	0.7503	0.6606	1.4071
9	0.6537	0.6567	0.6443	1.4380	1.0585
10	1.8519	1.2367	1.2333	0.8718	2.7243
11	1.1947	0.9122	0.8218	1.6219	1.4635
12	2.1617	1.5094	1.8185	1.5962	2.4254
13	2.6351	1.5181	1.8425	1.4782	1.9768
14	1.9851	1.2285	1.2920	1.2512	2.0523

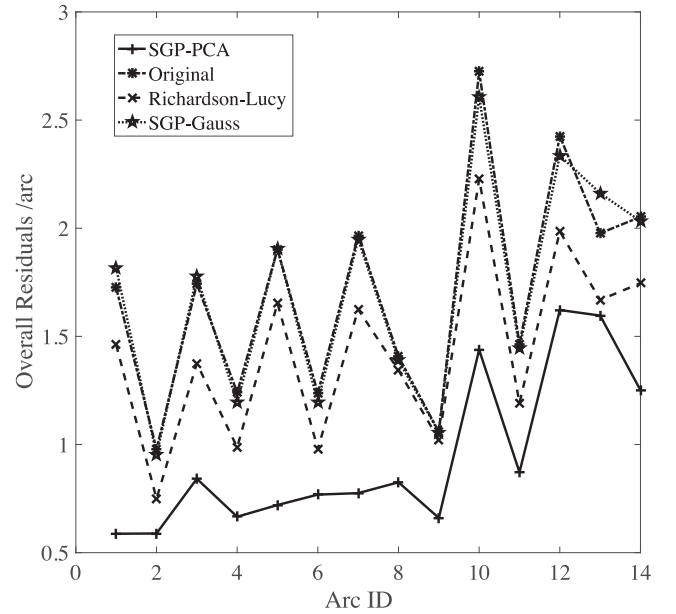


Figure 9. Astrometry accuracy for images restored with different methods for telescope A. SGP-PCA is our method, Original is the original image, Richardson–Lucy is the standard Richardson–Lucy method with a Gaussian PSF as the prior and SGP-Gauss is the SGP method with a Gaussian PSF as the prior. The size of the PSF we used in image restoration is 11 × 11 pixels.

increases. However, the astrometry accuracy will drop when the number of iterations is in excess of a certain number. This is due to the overfitting of the PSFs. Depending on the SNR of the image, the number of iterations when the astrometry accuracy stops increasing is around 10 to 300. According to this result, we will use 10 iterations for SGP-PCA in real applications for robustness.

To show the improvement in astrometry accuracy with our method, the overall residuals in different arcs processed by different methods are shown in Fig. 9. We also tested the SGP method with a Gaussian PSF as the prior PSF to complete the testing of our method. We labelled astrometry results from these data as SGP-Gauss. In this figure, we found that our method can provide at least 2 times improvement of astrometry accuracy than the other methods. The astrometry results from Richardson–Lucy method show the same trend with the original data, which indicates that the Richardson–Lucy method is more stable. The SGP-Gauss method gives the worst astrometry results, which indicates the importance of the prior PSF for our method.

This problem is notable for telescopes B and C, as shown in Figs 10 and 11. For telescopes B and C, the astrometry accuracy did not increase with our method or the Richardson–Lucy method, and in some arcs, the astrometry accuracy became even worse. We believe this is partly due to the image rotation of the telescope for the calibration data and partly due to different observation conditions between the observation data and the calibration data. The PSF classification results for telescope B in Fig. 12 show a very strong time-dependent variation of the PSFs in the whole image, which indicates that there are some temporal-variations of the PSFs in telescope B that are very serious and real-time calibration data are required. For telescope C, the classification results are similar. The results for telescopes B and C and that of SGP-Gauss method in telescope A indicate the importance of the calibration data in the SGP-PCA method.

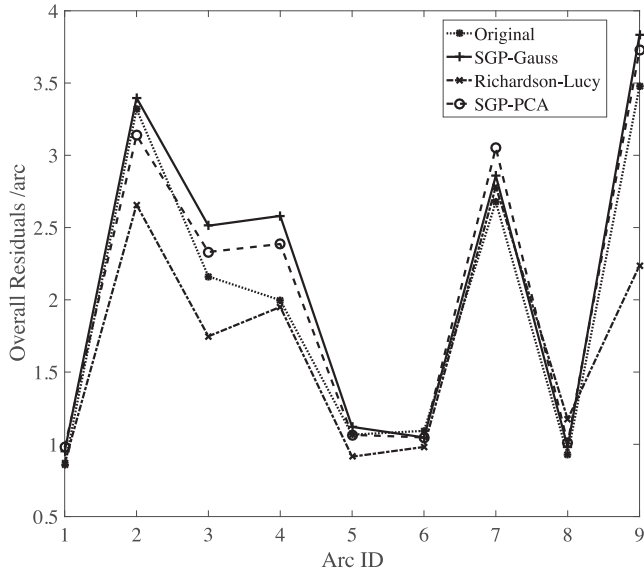


Figure 10. Astrometry accuracy for images restored with different methods for telescope B. SGP-PCA is our method, Original is the original image, Richardson-Lucy is the standard Richardson–Lucy method with a Gaussian PSF as the prior and SGP-Gauss is the SGP method with a Gaussian PSF as the prior. The size of PSF we used in image restoration is 11×11 pixels.

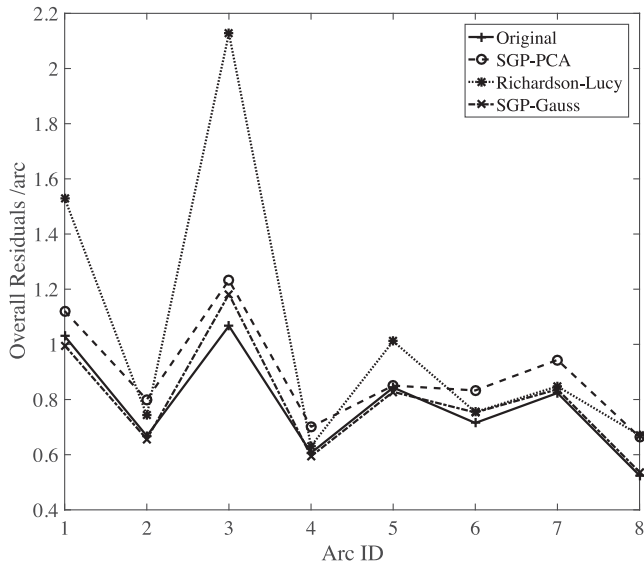


Figure 11. Astrometry accuracy for images restored with different methods for telescope C. SGP-PCA is our method, Original is the original image, Richardson–Lucy is the standard Richardson–Lucy method with a Gaussian PSF as the prior and SGP-Gauss is the SGP method with a Gaussian PSF as the prior. The size of the PSF we used in image restoration is 11×11 pixels.

Compared with the classical Richardson–Lucy method, the SGP-PCA method seeks a higher improvement in astrometry accuracy at the risk of errors due to an incorrect prior PSF. For this reason, the calibration data require detailed analysis before being applied in SGP-PCA and it is better to update the calibration data between observations.

4 CONCLUSIONS AND FUTURE WORK

In this paper, a new SGP-PCA deconvolution method is proposed. Our method identifies the PSF difference with SOM before

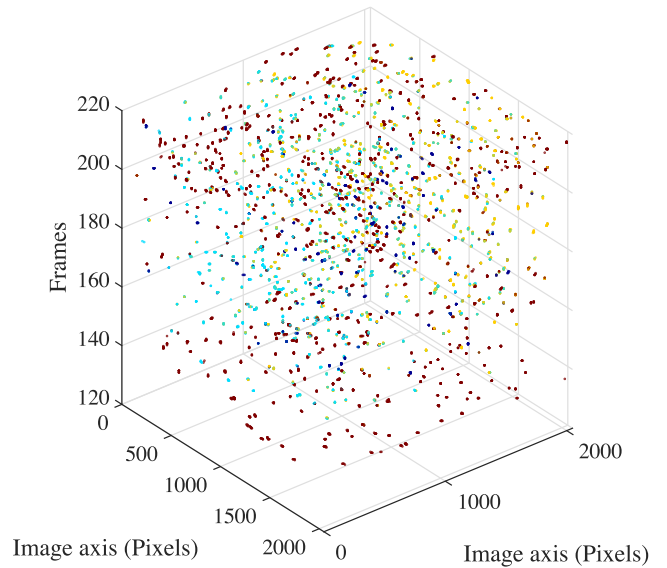


Figure 12. PSF classification results for the calibration data of telescope B. There are four classes of PSFs in this figure. A strong time-dependent variation can be observed.

blind deconvolution and sets an appropriate prior PSF for SGP-based blind deconvolution. This method can increase astrometry accuracy promisingly if the calibration data are adequate. To improve our method further, future work includes: (1) detailed analysis of a method of obtaining calibration data including cleaning of the calibration data, (2) a new PSF subtraction and normalization method that will be able to reduce magnitude difference effects in PSF classification to increase sample PSF coverage and (3) a density-based PSF classification algorithm with better computation efficiency and better performance for cluster detection.

ACKNOWLEDGEMENTS

This work is supported by the National Natural Science Foundation of China (grants 11403108, 11503018

and U1631133), the Youth Innovation Promotion Association of China Academy of Science (2015252) and Scientific and Technological Innovation Programs of Higher Education Institutions in Shanxi (2016033). PJ is supported by the China Scholarship Council to study at the University of Durham. The authors would like to thank Dr Alastair for proofreading the whole paper and helpful suggestions. The authors would also like to thank the anonymous reviewer and editor for the valuable comments, which helped to improve this manuscript substantially.

REFERENCES

- Ackermann M. R., Mcgraw J. T., Zimmer P. C., 2010, An Overview of Wide-Field-Of-View Optical Designs for Survey Telescopes
- Adams R., Bischof L., 1994, *IEEE Trans. Pattern Anal. Mach. Intell.*, 16, 641
- Adorf H.-M., Hook R. N., Lucy L. B., 1993, in Bely P. Y., Breckinridge J. B., eds, *Proc. SPIE Vol. 1945, Space Astronomical Telescopes and Instruments II*. SPIE, Bellingham, p. 75
- Armstrong D. J. et al., 2016, *MNRAS*, 456, 2260
- Ayers G. R., Dainty J. C., 1988, *Opt. Lett.*, 13, 547
- Babcock H. W., 1953, *PASP*, 65, 229
- Bailey S., 2012, *PASP*, 124, 1015
- Bertero M., Boccacci P., 2000, *A&AS*, 147, 323
- Brett D. R., West R. G., Wheatley P. J., 2004, *MNRAS*, 353, 369
- Britton M. C., 2006, *PASP*, 118, 885
- Burd A. et al., 2005, *New Astron.*, 10, 409
- Campisi P., Egiazarian K., 2016, *Blind Image Deconvolution: Theory and Applications*. CRC Press, Boca Raton, FL, p. 33487
- Carrasco Kind M., Brunner R. J., 2014, *MNRAS*, 438, 3409
- Chang C. et al., 2012, *MNRAS*, 427, 2572
- Ciliegi P. et al., 2014, *Proc. SPIE Vol. 9148, Adaptive Optics Systems IV*. SPIE, Bellingham, p. 91482O
- Desiderà G., Carbillat M., 2009, *A&A*, 507, 1759
- Fischer R. E., Tadic-Galeb B., Yoder P. R., Galeb R., 2000, *Optical System Design*. Citeseer. McGraw-Hill, New York
- Fors O., Nunez J., Otazu X., Prades A., Cardinal R. D., 2010, *Sensors*, 10, 1743
- Geach J. E., 2012, *MNRAS*, 419, 2633
- Gonzalez R. C., Woods R. E., 2002, *Digital image processing*, 2nd edn. Prentice Hall, NJ
- Grindlay J., Tang S., Los E., Servillat M., 2012, in Griffin E., Hanisch R., Seaman R., eds, *IAU Symp. 285, New Horizons in Time Domain Astronomy*. Kluwer, Dordrecht, p. 29 ([arXiv:1211.1051](https://arxiv.org/abs/1211.1051))
- Haykin B. S., 2010, *Neural Networks and Learning Machines*, 3rd edn. Prentice Hall, Upper Saddle River, NJ
- Høg E. et al., 2000, *A&A*, 355, L27
- Jee M. J., Tyson J. A., 2011, *PASP*, 123, 596
- Jee M. J., Blakeslee J. P., Sirianni M., Martel A. R., White R. L., Ford H. C., 2007, *PASP*, 119, 1403
- Jia P., Cai D., Wang D., 2014, *Exp. Astron.*, 38, 41
- Kaiser N. et al., 2002, in Tyson J. A., Wolff S., eds, *Proc. SPIE Vol. 4836, Survey and Other Telescope Technologies and Discoveries*. SPIE, Bellingham, p. 154
- Kelly B. C., Becker A. C., Sobolewska M., Siemiginowska A., Uttley P., 2014, *ApJ*, 788, 33
- Kohonen T., 1982, *Biolog. Cybernet.*, 43, 59
- La Camera A., Schreiber L., Diolaiti E., Boccacci P., Bertero M., Bellazzini M., Ciliegi P., 2015, *A&A*, 579, A1
- Lemaitre G. R., 2009, *Astronomical Optics and Elasticity Theory*. Springer, Berlin, Heidelberg
- Lukin V. P., 1995, *Atmospheric adaptive optics*. SPIE, Bellingham
- Lupton R., Gunn J. E., Ivezić Z., Knapp G. R., Kent S., 2001, in Harnden F. R., Jr, Primini F. A., Payne H. E., eds, *ASP Conf. Ser. Vol. 238, Astronomical Data Analysis Software and Systems X*. Astron. Soc. Pac., San Francisco, p. 269 ([astro-ph/0101420](https://arxiv.org/abs/astro-ph/0101420))
- Maehoenen P. H., Hakala P. J., 1995, *ApJ*, 452, L77
- Mast T. S., Nelson J. E., 1982, *Appl. Opt.*, 21, 2631
- Miller A. S., Coe M. J., 1996, *MNRAS*, 279, 293
- Núñez J., Núñez A., Montojo F. J., Condominas M., 2015, *Adv. Space Res.*, 56, 218
- Pascu D., Schmidt R. E., 1990, *AJ*, 99, 1974
- Piotrowski L. W. et al., 2013, *A&A*, 551, 1
- Popowicz A., Smolka B., 2015, *MNRAS*, 452, 809
- Popowicz A., Kurek A. R., Blachowicz T., Orlov V., Smolka B., 2016, *MNRAS*, 463, 2172
- Prato M., La Camera A., Bonettini S., Bertero M., 2013, *Inverse Prob.*, 29, 065017
- Smith W. J., 2000, *Modern optical engineering: the design of optical systems*. McGraw-Hill, New York
- Smithsonian Astrophysical Observatory 2000, *SAOImage DS9: A utility for displaying astronomical images in the X11 window environment*, *Astrophysics Source Code Library (ascl:0003.002)*
- Starck J. L., Pantin E., Murtagh F., 2002, *Publ. Astron. Soc. Pac.*, 114, 1051
- Stone R. C., 1989, *AJ*, 97, 1227
- Sun W., Yuan Y. X., 1997, *Springer Optim. Appl.*, 1, 103
- Sun R.-Y., Zhao C.-Y., 2014, *Res. Astron. Astrophys.*, 14, 992
- Theodoridis S., Koutroumbas K., 2008, *Pattern Recognition*, 4th edn. Academic Press, Cambridge, MA
- Vidal R., Ma Y., Sastry S., 2016, *Generalized Principal Component Analysis*. Springer-Verlag, Berlin, Heidelberg, New York
- Wang L. et al., 2009, in *astro2010: The Astronomy and Astrophysics Decadal Survey*. Science White Papers
- Wilson R. N., 1996, *Reflecting Telescope Optics I. Basic Design Theory and its Historical Development*. Springer, Berlin, Heidelberg
- Zhang Z.-P., Yang F.-M., Zhang H.-F., Wu Z.-B., Chen J.-P., Li P., Meng W.-D., 2012, *Res. Astron. Astrophys.*, 12, 212

This paper has been typeset from a $\text{\TeX}/\text{\LaTeX}$ file prepared by the author.